Showcasing research from Professor Richard A. Kirian's laboratory, Department of Physics, Arizona State University, United States of America.

Synchronized droplet nozzle for in-vacuum X-ray scattering experiments

This work presents the design and demonstration of a synchronized droplet injector for in-vacuum X-ray scattering experiments. By coupling 3D-printed gas dynamic virtual nozzles (GDVNs) with a piezo-driven cantilever, we achieve periodic droplet formation phase-locked to external triggers at 1 kHz. The system reduces sample consumption while providing larger effective scattering volumes compared to continuous microjets. Experimental results, supported by numerical simulations, show stable droplet synchronization in vacuum. Active feedback further enhances positional stability, enabling efficient, reproducible sample delivery for time-resolved X-ray studies.

Image reproduced by permission of Adil Ansari from *Lab Chip*, 2025, **25**, 6465.

As featured in:

See Adil Ansari *et al.*,
Lab Chip, 2025, **25**, 6465.

ROYAL SOCIETY
OF **CHEMISTRY**

rsc.li/loc

Check for updates

Synchronized droplet nozzle for in-vacuum X-ray scattering experiments†

Adil Ansari, [iD] *[acd] Roberto C. Alvarez,[c] Konstantinos Karpos,[c] Dimitra Manatou, [iD][ce] Garett Nelson,[c] Reza Nazari,[ac] Tanner Hochberg,[c] John Tamayo,[c] Hannah Nockideneh,[cf] Creed Hudson, [iD][c] Anubhav Singhal,[c] Divyanshu Tandon,[c] Natasha Forrand,[cf] Hao Hu,[cd] Diandra Doppler, [iD][db] Mukul Sonker, [iD][db] Alexandra Ros, [iD][db] Marcus Herrmann[a] and Richard A. Kirian [iD][cd]

Liquid microjets are widely used at X-ray free electron laser (XFEL) facilities to deliver a variety of samples to the pulsed X-ray focus for diffraction and spectroscopy experiments. Continuous jets waste sample between exposures, which is a major problem for many samples that are expensive or difficult to produce. Synchronizing microdroplets with the X-ray pulses can greatly improve the sample delivery efficiency by simultaneously reducing flow rate and producing a thicker sample. Here, we develop 3D-printed gas dynamic virtual nozzles (GDVN) designed to eject periodic droplets, and demonstrate synchronization with an external trigger of 1 kHz *via* piezoelectric transduction. A co-flowing helium sheath gas allows the droplets to eject into vacuum, which minimizes X-ray gas background scatter. Alternatively, the system can operate at atmospheric pressure without the need for humidity control. A control system enhances the synchronization such that 60% of droplet positions fall within 25% of the droplet diameter. Numerical simulations are presented that match well with experimental data and reveal recirculation patterns in the meniscus, along with a detailed view of the dynamics associated with onset of triggered synchronization. The system is designed such that it can be implemented at conventional end-stations at XFEL and synchrotron facilities with minimal modification.

1 Introduction

Precision in liquid sample delivery is critical in numerous applications, from biomedical diagnostics and drug discovery to advanced experimental techniques such as X-ray and electron spectroscopy, scattering and diffraction. The ability to generate droplets with precise volume, timing, and placement offers unique advantages for such applications, including enhanced efficiency, reduced sample consumption, and synchronization with downstream processes.[1] In many applications, an idealized droplets source is able to generate size-controlled, collimated spray of monodispersed droplets with high stability and periodicity over long periods of time.[2,3]

One application of such droplet sources is time-resolved small- and wide-angle X-ray scattering (TR-SWAXS). These techniques enable investigations of structural changes of proteins in solution, providing crucial insights into systems ranging from biomolecular conformational dynamics to nanoparticle assembly.[4,5] The quality of such measurements often hinges on the precision and reproducibility of the sample delivery system. Here, we present a droplet system designed for probing samples in solution with pulsed X-ray in vacuum, improving TR-SWAXS data collection and enabling broader applications in liquid-phase studies. Other related techniques such as photo-electron and X-ray spectroscopy would also benefit from such a droplet source.

1.1 Droplet production options

In 1878, Lord Rayleigh described the mechanism of breakup of liquid jets into droplets.[6] Elmqvist Rune patented a device capable of producing small droplets while Dr. Richard Sweet of Stanford University added a deflection mechanisms on these continuous droplets for early inkjet printing technology.[7,8]

[a] School for Engineering of Matter, Transport and Energy (SEMTE), Arizona State University, Tempe, AZ 85287, USA. E-mail: adil.ansari@asu.edu

[b] School of Molecular Sciences (SMS), Arizona State University, Tempe, AZ 85287, USA

[c] Department of Physics, Arizona State University, Tempe, Arizona 85287, USA

[d] Center for Applied Structural Discovery (CASD), Arizona State University (ASU), Tempe, AZ 85287, USA

[e] School of Biological and Health Systems Engineering (SBHSE), Arizona State University, Tempe, AZ 85287, USA

[f] Department of Physics, San Jose State University, San Jose, CA 95192, USA

† Electronic supplementary information (ESI) available: Fig. S1–S12. See DOI: https://doi.org/10.1039/d5lc00063g

On the basis of these technologies, drop-on-demand systems have been developed that produce droplets with diameters in the order of 10s of microns. This approach typically involves using piezoelectric actuation to force a volumetric displacement, resulting in on-demand droplet expulsion. Multiple companies (such as PolyPico, Scienion and MicroFab) have developed off-the-shelf drop-on-demand devices, several of which have been used for serial femtosecond crystallography (SFX) experiments at various XFEL facilities.[9–13] Some of these systems are readily available to XFEL facility users; for example, a Scienion drop-on-demand system has been integrated into the macromolecular femtosecond crystallography (MFX) end-station at LCLS.[14] This Scienion-based system typically operates in an atmospheric-pressure helium environment and requires humidity control in order to maintain a high degree of stability. Drop-on-demand systems have found applications beyond biological studies, including in the generation of microdroplet-based tin plasma sources for extreme ultraviolet (EUV) lithography, where precise droplet production is critical for efficient plasma generation in vacuum.[15] To the knowledge of the authors, commercially available droplet sources do not provide options for robust in-vacuum operation at the low flow rates that we desire for efficient TR-SWAXS studies. A central challenge with typical systems is the fact that the liquid meniscus is exposed to the vacuum, which causes freezing and hence device failure that usually requires breaking the vacuum in order to recover jet production. Freezing can be overcome by running a device at sufficiently high flow rate to produce a Rayleigh jet, which can then be triggered with a piezoelectric actuator, as demonstrated by Stan et al.[16] However, the comparably high flow rates and freezing issues are problematic for TR-SWAXS.

In this work, we demonstrate reliable in-vacuum, periodic droplet production at low flow rates via triggered dripping modes of GDVNs. GDVNs are appealing for our purposes because they were designed to operate in vacuum and they naturally produce periodic droplets when operated at sufficiently low liquid and gas flow rates. The droplet formation mechanism relies on a piezo-driven cantilever that induces periodic vertical oscillations in a lightweight GDVN, causing accumulated liquid to pinch off and eject as monodisperse droplets at a controlled frequency. Moreover, GDVNs have matured significantly since their inception; 3D printing has greatly enhanced the reproducibility of complex geometries.[17–19] and various upstream microfluidics can be integrated with the nozzle to allow for rapid mixing of biomolecules with substrates.[20,21] Droplets produced by GDVNs can be phase-locked with an external signal with various mechanisms that can be as simple as vibrating the nozzle. Doak et al. demonstrated the stimulation of Rayleigh breakup in liquid jets to generate droplets at frequencies upward of 50 kHz.[22] Our approach is based on similar methods disclosed by Doak, et al.,[23] albeit to force triggered formation of droplets rather than short jet filaments.

Martien et al. first explored the chaotic timing and dynamics of sequential drop formation in faucet dripping and Ambravaneswaran et al. investigated its physics using a one-dimensional slender-jet model.[24,25] Building on these studies, Clanet et al. described the transition from periodic drop formation to continuous jetting utilizing a critical We number.[26] This transition is also described by Herrada et al. for GDVNs where gas shear instead of gravity drives the liquid.[27] For GDVNs the liquid Weber number (We_l) in any mode can also be expressed as a function of liquid and gas flow rates:

$$We_l = \frac{1}{\sigma} \left(\frac{8\rho_l \Delta p_g^3}{\pi^2} \right)^{\frac{1}{4}} Q_l^{\frac{1}{2}} \tag{1}$$

where Δp_g is differential gas pressure across the nozzle gas orifice. As the jet length-to-diameter ratio decreases, liquid accumulates around the orifice due to surface tension, eventually forming a ligament. The ligament, with a higher length-to-diameter ratio, breaks up and is ejected. Sheath gas imparts kinetic energy to the accumulating liquid forming a standalone droplet, giving it more surface energy than an unforced accumulating mass. The liquid Reynolds number can be defined as such.

$$Re_l = \frac{2}{\mu_l} \left(\frac{\rho_l^3 \Delta p_g}{8\pi^2} \right)^{\frac{1}{4}} Q_l^{\frac{1}{2}} \tag{2}$$

Herrada et al. report that dripping is expected for liquid Reynolds numbers below 30 and Weber numbers below 1.5. In order to mitigate some of the key issues that have prevented routine TR-SWAXS measurements, we developed a new droplet-based sample injection system. It consists of a modification of existing gas-dynamic virtual nozzles (GDVNs) that enables them to operate in a controlled dripping mode resulting in reproducible droplets. The benefits of such an injector are that:

(1) The droplets are more than 10× thicker than an ordinary GDVN microjet resulting in 10× more signal scattered, (2) the sample consumption is orders of magnitude lower than an ordinary GDVN, (3) there are no issues with windows or diffusion of activated or radiation damaged sample that may be encountered with liquid cells such as thin glass capillaries, (4) the droplet system may be operated at multiple kilohertz to match detector data rates for the upcoming LCLS-II-HE facility, and (5) the system operates in vacuum as opposed to existing off-the-shelf micro droplet systems. Ultimately, the triggered dripping GDVN will allow for high signal levels with minimal sample consumption, which is critical for samples that are available only in low abundance.

2 Materials and methods

2.1 Droplet device design

An illustration of the device used for droplet production is shown in Fig. 1a. Synchronized, periodic droplets are
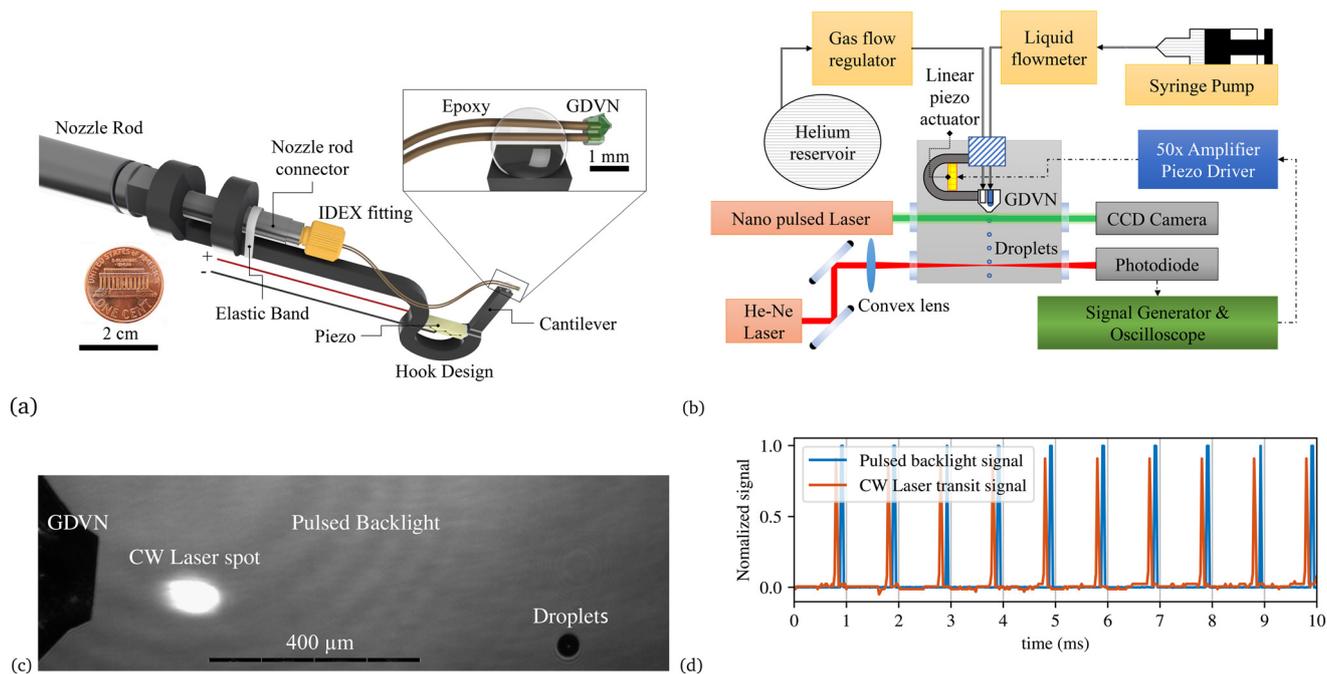
Fig. 1 (a) 3D rendering of the design used to mount a GDVN to a piezoelectric-driven hook-shaped cantilever. The cantilever is mounted to a conventional nozzle rod that allows for insertion into a vacuum chamber *via* conventional load-lock system. The gas and liquid lines connecting to the nozzle are given slack to allow for unbridled motion. The GDVN geometry is shown greater detail in Fig. S1.† (b) Schematic of experimental setup as described in section 2. (c) Strobed image of ~30 droplets of 51.1 ± 2.6 μm diameter ejected from the GDVN with a CW helium–neon laser spot on the droplet stream. The nano pulsed blacklight may be synchronized to the X-ray signal for droplet positioning. (d) Droplet transit signal along with 1 kHz trigger signal.

achieved with a GDVN attached to a cantilever with a resonant frequency near 1 kHz. The cantilever extends from a hook that holds a linear piezoelectric transducer to create periodic motion. Under certain conditions, the droplets are phase locked to the periodic motion. The GDVN and hook are attached to a standard nozzle rod[28] that allows the injector to be inserted into the chamber *via* a load-lock system that avoids breaking vacuum. Since acceleration increases with frequency squared, the effectiveness of the cantilever mechanism likewise increases with frequency. The cantilevers were 3D printed using Formlabs 2 stereolithography (SLA) printers (USA) with Tough 2000 or Rigid 4 K resins, or on Ultimaker 3 (Netherlands) with PLA filament. GDVNs were fabricated using a Nanoscribe Photonic Professional GT 3D printer (Germany) with two-photon polymerization of Nanoscribe IP-S resin (Germany) and developed in Kayaku SU-8 developer (USA). Vacuum tests at approximately 10^{-5} mbar indicate that the outgassing from this resin is not significant when compared to the gas load associated with the GDVN. A standard dry-scroll pump (Edwards nXDS10i, UK) was used for producing the vacuum. A schematic of the system that monitors and controls the droplets is shown in Fig. 1b. The GDVN helium mass flow rate is measured and controlled with a Bronkhorst EL-Flow device. The water volumetric liquid flow rate is controlled with a syringe pump (Harvard Apparatus Pump 33 DDS, USA) and measured with a flowmeter (Sensirion SLG0075, Switzerland). Deionized (DI) water

filtered through reverse osmosis (RO) filters, as well as aqueous suspensions of 50 nm polystyrene (PS) spheres (Polysciences Polybead Carboxylate Microspheres 0.05 μm, USA) diluted in DI water were liquids used as samples in droplets. Droplets are imaged stroboscopically with a CMOS camera (Thorlabs DCC3240M, USA) backlit by a pulsed laser (Thorlabs NPL52C, USA) with 520 nm wavelength and 100 ns pulse duration. A continuous helium–neon 633 nm laser is focused on the droplet stream. The transit of the droplets across this continuous laser beam is detected by a photodiode (Thorlabs DET10A, USA), which allows for continuous monitoring of the phase and frequency of the droplets. A 5 V arbitrary function generator (Digilent Analog Discovery 2, USA) feeding into a 50× amplifier (Advanced Energy Trek Model 2100HF, USA) drives the piezoelectric transducer. Both the stroboscopic imaging system and the piezoelectric driver are triggered by an external signal that emulates the arrival time of the X-ray pulses. Notably, this configuration allows for slight drifts in the X-ray pulse frequency/phase without disrupting the phase-locking of the droplets with the X-ray pulses. In order to enable programmatic control and active feedback capabilities to the system, an oscilloscope (Digilent Analog Discovery 2, USA) digitizes the analog signals from the X-ray signal and the droplet transit signal. The analysis of these signals and the active feedback system is discussed further in section 3.3.2. The use of a single Analog Discovery 2 device to record both input signals and produce the piezoelectric

driving signal simplifies synchronization with the external X-ray signal.

2.2 Device operation

The gas and liquid flows were initiated to commence the droplet production. With the GDVN in vacuum, the gas flow must be started before the liquid flow in order to avoid liquid freezing. The flow rates were chosen according to GDVN natural dripping-mode characterizations discussed in section 3.1. Once the droplets became visible on the camera, the mirrors for the He–Ne laser were adjusted such that the laser beam overlapped with the droplets at a fixed spatial location. This overlap was achieved by observing the laser spot with the camera as shown in Fig. 1d. The position of the convex lens was then adjusted to ensure that the laser was tightly focused on the droplet stream. A sufficiently tight focus (usually 200 microns or less) was determined by observing the photodiode signal, which exhibited strong periodic dips upon successful alignment. The Fourier transform of the droplet signal was used to monitor the dripping frequency.

With the optics aligned, the liquid flow rate was fine-tuned such that the dripping frequency was close to the desired frequency (1 kHz in most cases). Once the natural frequency was sufficiently close, the piezoelectric transducer was activated. Lock-in was evident when the droplet signal appeared to be static with respect to the X-ray signal. A stroboscopic image resulting from successful phase-locked droplets is shown in Fig. 1c. The phase of the droplets was monitored quantitatively by computing cross correlations between the digitized droplet and the X-ray signals.

2.3 Active feedback system

Although the phase of the piezo driving voltage correlated strongly with the phase of the droplet signal, the positional stability of the droplets was not always sufficient for our anticipated TR-SWAXS measurements. We therefore constructed a proportional-integral-derivative control system to further stabilize the phase of the droplets. To measure the droplet phase, N samples of the clock trace signal $c(t)$ were cross-correlated with the droplet transit signal $d(t)$:

$$R_n = \sum_i^N c(t_i) d(t_i - n\delta t) \tag{3}$$

Each clock/droplet trace consisted of multiple cycles (approximately 10). The cross-correlation R_n was ascertained and its maximum peak position was used to compute the droplet phase. The update rule for the phase set-point of the piezoelectric driver signal was

$$\Phi_{k+1} = \Phi_k + K_p(\phi_{desired} - \phi_k) \tag{4}$$

where $\phi_{desired}$ is the desired droplet phase, Φ_k is the kth driver phase set-point, ϕ_k is the kth measured droplet phase, and K_p is the proportional gain of order 1.

3 Results

3.1 Natural droplet frequencies

Ideally, GDVNs would be capable of producing stable, periodic drops of the desired frequency prior to the activation of the piezo driver. Since different samples require different solutions, and each solution has different liquid properties, characterization of droplet generation is imperative for selecting the proper GDVN and injection conditions. To begin maximizing the applicability of this injection method, two different nozzle designs, N50 and N100, depicted respectively in Fig. S1,† were characterized.

The observed natural dripping landscape for the (I) N50 and (II) N100 GDVN are detailed in Fig. 2a and b, where the He was varied from 0.5 to 3 mg min^{-1} and the DI water flow rate varied from 1 to 9 μL min^{-1}. As both the flow rates increased, so did the frequency, indicated by the color bar. Throughout the parameter sampling space, both nozzles remained in stable dripping modes, however, due to the smaller gas orifice of the N50 nozzle, higher droplet frequencies were achieved compared to the N100. Two specific dripping conditions, indicated by a red X on plot (I), were numerically simulated and the results will be discussed in section 4.

3.2 Synchronized droplet results

During synchronization tests, the piezo was driven with a variety of waveforms, all with a peak-to-peak amplitude of 100 V. It was concluded that a sine function worked best for the N50 GDVN, whereas a ramp-down function worked best for the N100 GDVN. The vacuum chamber pressure was 0.1 mbar. 1 kHz dripping for N50 was observed when liquid and gas flow rates were 1.2 μL min^{-1} and 0.9 mg min^{-1}, respectively. For the N100, the same frequency droplets were observed when the liquid and gas was around 4.2 μL min^{-1} and 1.0 mg min^{-1}, respectively. The droplets resulting from the N100 and N50 GDVNs were 32.8 ± 6.4 μm and 51.1 ± 2.6 μm respectively, corresponding to droplet volumes of 18.5 ± 1.7 pL and 70.0 ± 4.2 pL.

Stroboscopic images revealing the droplet expulsion dynamics were obtained when varying the phase of the driving 1 kHz signal, and outlined in Fig. 2. As the images progress along the few hundred ţs time frame, the liquid meniscus stretches along the Z-position from the nozzle maintaining a connection to the GDVN liquid line until it collapses into smaller droplets through Rayleigh breakup. The resulting droplets often appear to be stacked vertically by size, and merge into the bottom most, largest droplet due to the smaller droplets having a higher drag acceleration with help from wake velocity fields. Fig. S2† shows the GDVN oscillation motion and droplet ejection relative to the motion, as determined from the stroboscopic image sequence. The droplets decouple from the GDVN when the nozzle acceleration is opposite the direction of the liquid flow.
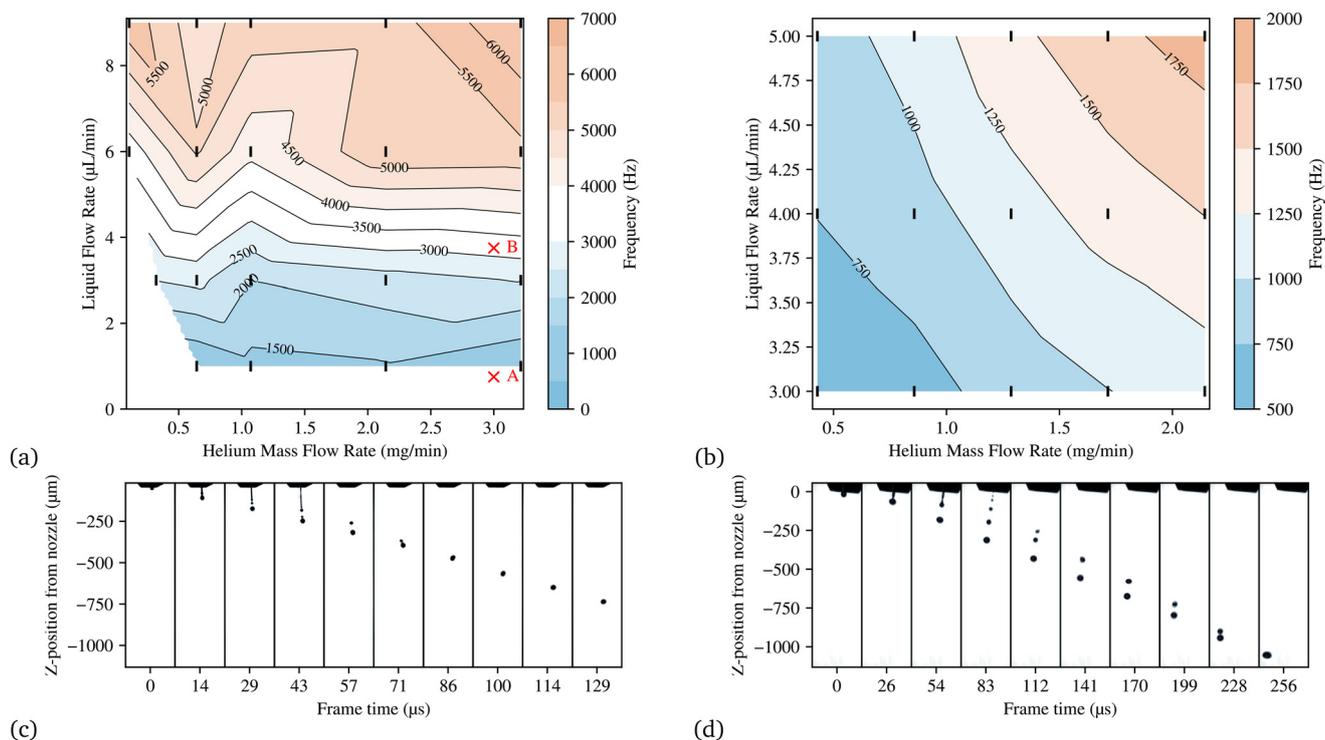
Fig. 2 (a) Natural dripping frequency of design N50 in vacuum. Red × symbols indicate simulations discussed in section 4, with point A at 950 Hz and point B at 4500 Hz. (b) Natural dripping frequency of design N100, which has a wider orifice. (c and d) Droplet ejection dynamics of designs N50 and N100, respectively. The leading droplet velocities are 5.6 m s^{-1} and 4.2 m s^{-1}.

Droplet synchronization is further seen with the droplets transiting the helium–neon laser producing a nearly 15 mV drop in the photo-diode signal with periodic repetition. The Fast Fourier transform (FFT) of this is shown in Fig. S3.† The signal's FFT shows non-zero spikes at every multiple of 1 kHz due to orthogonality.

3.3 Long-term stability

Droplet jitter and drift are two observed behaviors that affect the quality of TR-SWAXS data. Jitter can be understood as the stochastic variation in sequential droplet positions on rapid timescales (~1 ms in the case of 1 kHz frequency). Drift can be understood as the systematic variations in sequential droplet positions on larger timescales (seconds). Droplet drift is largely due to GDVN flow rate drift and can be reduced with an active feedback system, whereas jitter reduction will likely require future investigations that vary the nozzle geometry and/or triggering mechanisms.

3.3.1 Flow rate considerations. While the gas flow rates were very stable due to the embedded control system in the Bronkhorst device, liquid flow rates driven by the syringe pump were observed to drift by as much as ±30% over periods of 10s of seconds, as shown in Fig. S7.† In Fig. S8,† it is shown that the droplet phase, shown with a water fall plot (1D projections of 2D droplet images), is strongly affected by such liquid flow rate drifts.

Imperfections in the syringe pump mechanism or flow resistance variations are the typical cause of drift. Increasing the pressure capacitance in the liquid flow circuit can help smooth out flow rate variations; for example, simply introducing a bubble in the syringe can help, though the responsiveness of the system is reduced. An additional problem is the formation of bubbles in the liquid line of the GDVN due to the low pressure that the liquid is subjected to as it reaches the gas cavity. The interface between the glass capillary and the 3D printed GDVN is a common gas bubble nucleation spot, likely due to the sharp edges of the glass capillary. Choked helium flow rate of 1 mg min^{-1} through an 80 μm orifice results in a pressure of approximately 36 mbar, where water's boiling point is 25 °C. Dissolved gases in the liquid exacerbate the bubbling problem, but degassing the sample with a vacuum and/or ultrasonic waves typically had a positive impact on the stability of the flow rate (Fig. S7†).

Additional studies illustrate the impact of different liquid properties viscosity, ionic strength, and surface tension on the dripping behavior of the system, as shown in Fig. S4–S6,† respectively. In all cases, synchronization with the external trigger was achieved successfully. The use of a 20% glycerol solution (higher viscosity)[44] and a 75 mM NaCl solution (higher ionic strength) did not exhibit significantly different behavior compared to water, and no visible residue or salt buildup was observed under vacuum
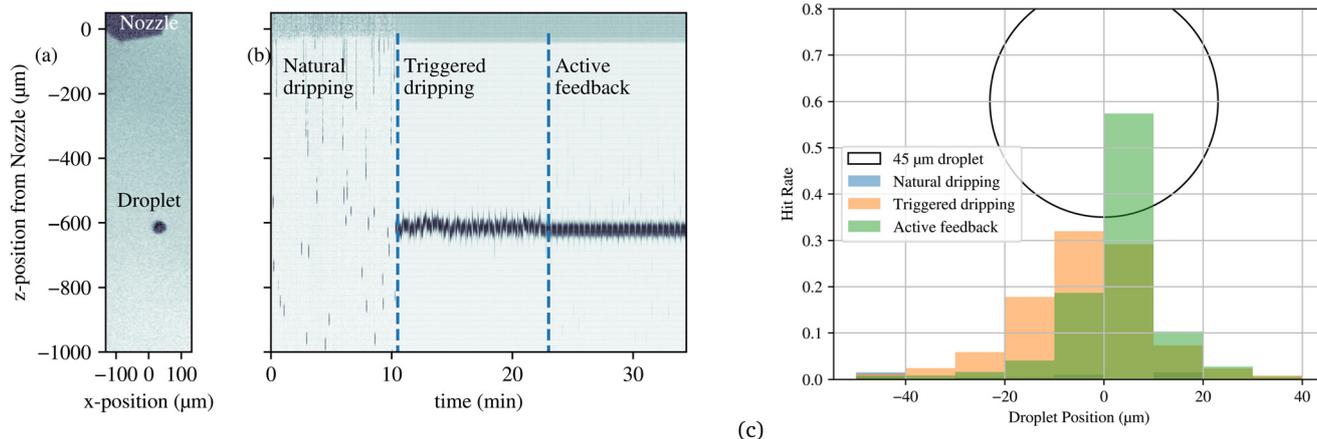
Fig. 3 (a) 45 μm diameter droplets produced at a frequency of 1 kHz with gas flow rate 0.8 mg min⁻¹ and liquid flow rate of 3 μL min⁻¹. (b) A sequence of corresponding 1D projections of the 2D images illustrating droplet position variations under the conditions of natural dripping (first ~10 min), triggered dripping (second ~10 min) and triggered dripping with active feedback (final ~10 min). (c) Histogram of droplet positions determined from 2D images. The circle represents the droplet size for comparison to the position distribution. The natural dripping hit rate is near zero and hence not visible.

conditions. In contrast, lowering the surface tension using isopropyl alcohol produced a noticeably longer liquid filament prior to droplet detachment. Subharmonic generation of order one-half was also observed for this case. These results were obtained using the same device described in Fig. 3. None of these property variations resulted in the elimination of degassing.

3.3.2 Droplet stability with control system. Fig. 3b shows waterfall plots of an experiment with natural dripping, triggered dripping and triggered dripping with active feedback. The waterfalls were created by projecting a sequence of 2D images (each with one back-illumination flash) into a series of 1D traces. The sample used here is 50 nm polystyrene spheres with a concentration of 0.3% v/v (4 mg mL⁻¹) in deionized water. Sample flow rate was 3 μL min⁻¹ and He gas flow rate was 0.86 mg min⁻¹. The K_p value, as defined in eqn (4), was set to 0.75.

Fig. 3c shows that the majority of the droplet positions are within a quarter of the droplet diameter when the ejection is phase-controlled with active feedback, which is a 2-fold improvement over the case without active feedback. Fig. S9† shows the long term stability of triggered droplets with active feedback on droplet phase. There are periodic drifts over 30 seconds likely due to degassing. Less than 200 μL of sample was used during that hour.

3.4 Operation at atmospheric pressure

Although the results presented above were acquired in a vacuum environment (0.1 mbar helium), we obtained similar results when operating the system at atmospheric pressure. While commercially available systems are also capable of producing similar results, it is noteworthy that the use of a GDVN avoids the need for humidity control, which can have dramatic impacts on droplet stability and also increases X-ray background scatter. Additionally, the formation of bubbles in

the GDVN liquid line were not observed when operating at atmospheric pressure.

4 Numerical simulation

In this section, we explore the simulation of GDVN dripping to achieve a deeper understanding of the dripping phenomenon. The simulations focus on the smaller nozzle (design N50), due to the increased stability from lower Reynolds numbers. We will examine the flow features from this nozzle geometry and compare them with experimental dripping results both with and without the piezo-driven nozzle motion.

4.1 Numerical setup to simulate GDVN dripping

For ideal gases, the incompressible flow assumption typically holds when Mach number is less than $\frac{1}{3}$.[29] With a 50 μm nozzle orifice and a gas flow of 3 mg min⁻¹, the average flow velocity of helium is approximately 130 m s⁻¹, which is under Mach 0.3 for helium. This incompressible assumption renders $\vec{U}$ divergence free:

$$\nabla \cdot \vec{U} = 0. \tag{5}$$

The density scalar ρ is transported along $\vec{U}$ and the mass-continuity equation is

$$\frac{\partial p}{\partial t} + \nabla \cdot \left(p \vec{U} \right) = 0. \tag{6}$$

The Navier–Stokes equations describe the temporal evolution of a fluid momentum vector field ($\rho \vec{U}$):

$$\frac{\partial}{\partial t}\left(\rho \vec{U}\right) + \nabla \cdot \left(\rho \vec{U} \otimes \vec{U}\right) - \nabla \cdot \left(\mu \left(\nabla \vec{U} + \left(\nabla \vec{U}\right)^T\right)\right) \tag{7}$$
$$= -\nabla p + \sigma \kappa \hat{n} \delta \left(\vec{x} - \vec{x}_f\right).$$

where μ is the temperature-independent-viscosity. The last term represents the surface tension force vector and is

proportional to the σ and the curvature (κ) of the interface and is only active at spatial coordinates where the interface is present ($\vec{x}_f$). For our simulations of dripping with helium sheath gas, σ is assumed to be independent of the pressure and temperature of the fluid medium. Eqn (5)–(7), end up forming 5 equations that are closed by five variables $\vec{U}$ (U_x, U_y, U_z), p, and ρ.

Due to axisymmetry, the 3 dimensional Navier–Stokes equations can simulated on a collapsed axisymmetric mesh to simplify the computation. A 2D hexahedral conformal mesh was generated using a Python code called SwiftBlock with a user interface (UI) on Blender[30] as seen Fig. S10.† Then, this mesh was made axisymmetric in OpenFOAM with wedge boundary conditions on the two radial side faces of the sector aligned along the axis of symmetry. Moving mesh[31] is implemented for sinusoidal motion triggering and this is convenient because the motion is aligned with the axis of axis-symmetry. The entire mesh oscillates sinusoidally with a maximum velocity of 0.0314 m s^{-1}, and a largest time-step constraint of 5 μs to ensure CFL condition compliance. Solver uses isoAdvector[32] which tracks geometric liquid distribution within cells to solve time evolution of liquid–gas interface.[33,34] The numerical method for simulating surface tension and surface wetting implemented in OpenFOAM is described by Brackbill *et al.* 1992.[35]

4.2 Numerical results

In this study, the GDVN simulation is made to operate at low liquid and gas flow rates, enabling the production of droplets instead of continuous jets. The mesh resolution near the nozzle orifice was set to approximately 500 nm. The liquid phase, represented by water, had a density of 1000 kg m^{-3} and a viscosity of 1 cP. The gas phase, modeled as helium, had a density of 0.179 kg m^{-3} and a viscosity of 19.6 μPa s. By setting the liquid flow rate at 0.750 μL min^{-1} and the gas flow rate at 3 mg min^{-1}, the simulation revealed a periodic dripping behavior with a frequency of approximately 950 Hz. This is close enough for synchronization tests. As such, the gas phase has Re of approximately.[20] Using eqn (2) and (1), the non-dimensional parameters were ascertained. The ΔP is determined from the mass flow rate. This has been validated in our previous publication.[36] The We number is 0.8. The Re of liquid after exiting the liquid line is 6.

4.2.1 Synchronization tests. Further investigation focused on the effect of vertical sinusoidal motion on droplet production. The simulation revealed that when the GDVN was subjected to a 1 kHz sinusoidal motion with an amplitude of 5 ʈm, the droplet production rate synchronized with the frequency of the sinusoidal motion. However, due to the inherently chaotic nature of fluid dynamics, the precise positions of the droplets at each 1 ms interval were slightly offset and unpredictable. This partly was due to the fact that the natural dripping was 950 Hz at the set flow rate. Fig.
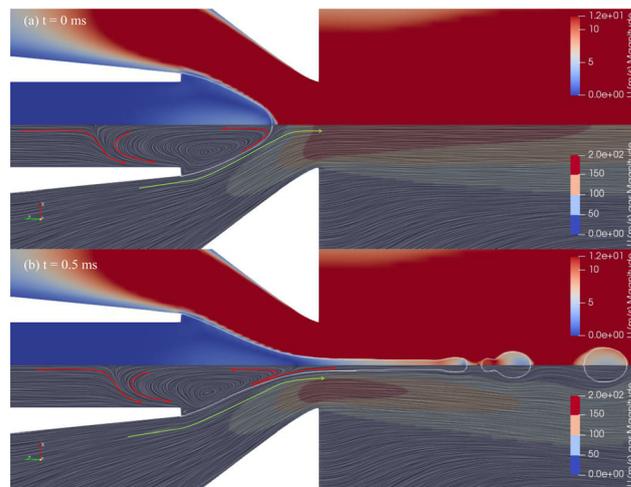

Fig. 4 Fluid velocity profile during dripping (b) and half way before next dripping event (a) with forced natural dripping at 1 kHz.

S11† suggests that forced motion at 1 kHz created bimodal distribution of droplet position within the limited number of periods simulated. The likelihood of such a configuration out sheer randomness is quite unlikely. Such phenomenon has been observed experimentally. A positive take-away from that simulation is that synchronization only takes about 3 ms when starting or changing trigger. This indicates that <1% of the shots will be lost due to phase correction. Fig. 4 sheds light into the fluid dynamics of the GDVN dripping. It indicates that the recirculation remains active during and in between dripping events. This axisymmetric recirculation is a well-documented feature in flow-focusing GDVN jets,[37,38] and our own simulations[33] confirm that it arises from the interplay of continuity, viscosity, and surface tension. Since the channel Reynold's number $\left(\dfrac{\rho U D}{\mu}\right)$ is 0.3 one can be reasonably certain that there would be no turbulence to add chaos to the dripping.

4.3 Simulation and experimental data comparison

We present the contours of the natural dripping frequency, as depicted in the Fig. 2a. The GDVN simulation results for liquid and gas flow rates of 0.75 μL min^{-1} and 3 mg min^{-1} are overlaid on the same plot. The simulation yields a frequency of 950 Hz, which falls beyond the range of the collected data. However, this value aligns well with the extrapolated trend derived from the available data. Another data point that was explored was near same gas flow rate but 5× higher liquid flow rate (3.75 μL min^{-1}). The outcome of the simulation is around 4500 Hz. However, a simulation study on the effect on contact angle yielded quite a few different results indicating dripping frequency reduces by as much as 10% with increase in contact angle to 90 degrees (Table 1). It is relevant that the contact angle of cured photo-polymers changing significantly over time further explaining the disagreement.[39]
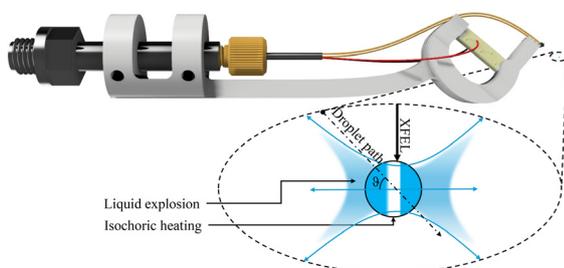
Table 1 Numerical results of dripping frequency as a function of contact angle

Contact angle (degrees)	Dripping frequency (Hz)
30	4528
50	4520
70	4493
90	3993

5 Discussion

Compared to microjets, droplets have a roughly 10× larger diameter while consuming 10× less sample. As a result, the in vacuum droplet system presented here holds great promise for achieving 100-fold efficiency boosts in TR-SWAXS measurements at facilities such as the LCLS and CXLS. However, this improvement remains to be demonstrated with X-ray. One anticipated challenge is the surface scatter created when the X-ray beam intercepts the liquid–vacuum interface, which is a complication that often arises when using small (~4 µm) liquid jets. However, the large size of the droplets should mitigate surface scatter issues to a large degree, provided a sufficiently tight X-ray focus of approximately 1 µm. Droplet position variance might need to be reduced further than demonstrated here, which can be achieved by modifying the triggering mechanism – for example, a volume displacement trigger as opposed to whole-nozzle vibrations could help. Replacement of the passive syringe pump with an active liquid flow controller (as was used for the gas flow in this study) will also have a significant positive effect on droplet stability. Irrespective of such improvements, occasional poorly-timed droplets should be expected, but this issue can be minimized by storing the droplet-transit signal along with optical droplet images in the data stream such that they can be used to exclude outliers from the X-ray analysis. An additional challenge that will arise in the case of large XFELs is the explosive debris produced by the high energy X-ray pulses. In certain conditions, the nozzle tip may accumulate non-volatile debris over time, which can effectively change the geometry and hydrophilicity of the nozzle tip. It remains to be determined if this issue is significant, but we expect it to be less severe than in the case

of commercial drop-on-demand devices since the liquid orifice is shielded by the GDVN sheath-gas cavity, and the active feedback system should be able to compensate for the gradual drift. It may be helpful to intentionally produce pairs of drops, with the second drop serving to shield the nozzle from the high-speed debris. A design modification to point the GDVN at an angle of less than 90 degrees with respect to the X-ray beam would reduce the issues of both droplet jitter and explosive debris. When projected at an angle of θ, the effective jitter of the droplets would be reduced by a factor of $\cos\theta$, and the explosive debris would largely miss the nozzle since they are mostly directed within 40 degrees from perpendicular to the X-ray beam.[40] Fig. 5 shows such a modification.

Since the droplets experience a vacuum environment, they will cool before reaching the X-ray interaction point. Previous studies of 40 µm water drops ejected into vacuum show that they reach super-cooled temperatures and begin freezing after ~6 ms exposure to vacuum.[41,42] In our case, the droplets move at speeds of 4 m s⁻¹ which corresponds to vacuum exposure times of less than 250 µs with an interaction point within 1 mm distance from the nozzle tip.

Implementation of the droplet system into existing XFEL beamlines will be straightforward, provided that the beamline utilizes a load-lock system with typical dimensions. The hook/cantilever fits through a standard KF25 quickflange fitting, and should fit within most debris shrouds with conical exit apertures for the scattered X-ray. Our CFD simulations suggest that synchronization occurs within just a few milliseconds, meaning that only a minimal number of droplets should be lost during phase changes in the control system. Furthermore, the simulations indicate that re-circulation remains active even when the GDVN is not ejecting any liquid. This could potentially be used as a pre-mixer before droplet ejection in mixing experiments.

6 Conclusion

This study was motivated by a need to reduce sample consumption for in-vacuum time-resolved X-ray scattering experiments with biomolecules. We characterized dripping modes of gas-dynamic virtual nozzles, which produce quasi-periodic droplets in vacuum at a range of frequencies. The droplets were synchronized with an external trigger by vibrating the nozzle at 1 kHz with a piezoelectric transducer. An active feedback system was developed to control against drifts in droplet position induced by flow-rate instabilities. The system was shown to be stable over long periods of time when delivering non-volatile samples. In the case of 45 µm diameter droplets, 60% of the droplets were positioned within 25% of the droplet diameter. If utilized for time-resolved X-ray solution scattering, the boost in sample utilization efficiency (defined as the number of scattered photons per sample volume) is predicted to be 100-fold higher than conventional microjet- or capillary-based sample delivery systems, leading to significantly faster data collection

Fig. 5 Modification of 'hook' structure from Fig. 1a to produce droplets at an angle. The zoomed inset illustrates the explosion plume caused by high-pulse-energy XFELs. With sufficiently large angle θ, these explosion debris will not intercept and accumulate on the nozzle.

and reduced time required for sample preparation. The system can operate in vacuum or at atmospheric pressure, without the need for humidity control. Computational fluid dynamics simulations were presented and shown to match well with experimental results. The simulations revealed recirculation patterns in the liquid meniscus along with a detailed view of the synchronization process, both of which are extremely difficult to observe experimentally due to the small size of the liquid meniscus located inside the nozzle.

Data availability

The raw data is available on request. The code used in this study are openly accessible to support the reproducibility and transparency of our research. The code pertaining to image analysis of dripping characteristics, including temporal dynamics, droplet size distributions, and phase diagrams, can be found in the Gitlab repository: **https://gitlab.com/aansari21/syncronized-dripping-in-vacuum**. The same repository also contains simulation files for OpenFOAM to solve the GDVN dripping used for comparison.

Author contributions

R. K. conceived and supervised the overall project. A. A. led the device design, experimental design, data collection, data analysis, simulations, and manuscript writing. R. N. developed the microfluidic nozzles, contributed to natural dripping characterization, and was involved in triggering mechanism discussions. R. N., R. A., K. K., and G. N. were involved in early experimentation. A. A., D. D., M. S., H. H., and D. M. contributed to nozzle printing and fabrication. T. H., J. T., H. N., C. H., D. T. and A. S. were involved in device development and data collection. A. A., N. F., and R. K. worked on control system implementation. D. D., M. S., A. R., and M. H. reviewed and revised the manuscript text.

Conflicts of interest

There are no conflicts to declare.

Acknowledgements

Notes and references

1 L. Shang, Y. Cheng and Y. Zhao, *Chem. Rev.*, 2017, **117**, 7964–8040.

2 A. M. Gañán-Calvo, *Phys. Rev. Lett.*, 1998, **80**, 285.

3 W. C. Hinds and Y. Zhu, *Aerosol technology: properties, behavior, and measurement of airborne particles*, John Wiley & Sons, 2022.

4 R. Neutze, *Philos. Trans. R. Soc., B*, 2014, **369**, 20130318.

5 F. Schulz, I. Lokteva, W. J. Parak and F. Lehmkühler, *Part. Part. Syst. Charact.*, 2021, **38**, 2100087.

6 L. Rayleigh, *Proc. London Math. Soc.*, 1878, **1**, 4–13.

7 E. Rune, Measuring instrument of the recording type, *US Pat.*, 2566443, 1951.

8 R. G. Sweet, *Rev. Sci. Instrum.*, 1965, **36**, 131–136.

9 F. Mafuné, K. Miyajima, K. Tono, Y. Takeda, J.-Y. Kohno, N. Miyauchi, J. Kobayashi, Y. Joti, E. Nango, S. Iwata and M. Yabashi, *Acta Crystallogr., Sect. D: Struct. Biol.*, 2016, **72**, 520–523.

10 C. G. Roessler, R. Agarwal, M. Allaire, R. Alonso-Mori, B. Andi, J. F. Bachega, M. Bommer, A. S. Brewster, M. C. Browne, R. Chatterjee, E. Cho, A. E. Cohen, M. Cowan, S. Datwani, V. L. Davidson, J. Defever, B. Eaton, R. Ellson, Y. Feng, L. P. Ghislain, J. M. Glownia, G. Han, J. Hattne, J. Hellmich, A. Héroux, M. Ibrahim, J. Kern, A. Kuczewski, H. T. Lemke, P. Liu, L. Majlof, W. M. McClintock, S. Myers, S. Nelsen, J. Olechno, A. M. Orville, N. K. Sauter, A. S. Soares, S. M. Soltis, H. Song, R. G. Stearns, R. Tran, Y. Tsai, M. Uervirojnangkoorn, C. M. Wilmot, V. Yachandra, J. Yano, E. T. Yukl, D. Zhu and A. Zouni, *Structure*, 2016, **24**, 631–640.

11 F. D. Fuller, S. Gul, R. Chatterjee, E. S. Burgie, I. D. Young, H. Lebrette, V. Srinivas, A. S. Brewster, T. Michels-Clark and J. A. Clinger, *et al.*, *Nat. Methods*, 2017, **14**, 443–449.

12 A. Butryn, P. S. Simon, P. Aller, P. Hinchliffe, R. N. Massad, G. Leen, C. L. Tooke, I. Bogacz, I.-S. Kim, A. Bhowmick, A. S. Brewster, N. E. Devenish, J. Brem, J. J. A. G. Kamps, P. A. Lang, P. Rabe, D. Axford, J. H. Beale, B. Davy, A. Ebrahim, J. Orlans, S. L. S. Storm, T. Zhou, S. Owada, R. Tanaka, K. Tono, G. Evans, R. L. Owen, F. A. Houle, N. K. Sauter, C. J. Schofield, J. Spencer, V. K. Yachandra, J. Yano, J. F. Kern and A. M. Orville, *Nat. Commun.*, 2021, **12**, 4461.

13 T. R. M. Barends, B. Stauch, V. Cherezov and I. Schlichting, *Nat. Rev. Methods Primers*, 2022, **2**, 59.

14 S. Boutet, A. E. Cohen and S. Wakatsuki, *Synchrotron Radiat. News*, 2016, **29**, 23–28.

15 O. Versolato, J. Sheil, S. Witte, W. Ubachs and R. Hoekstra, *J. Opt.*, 2022, **24**, 054014.

16 C. A. Stan, D. Milathianaki, H. Laksmono, R. G. Sierra, T. A. McQueen, M. Messerschmidt, G. J. Williams, J. E. Koglin, T. J. Lane, M. J. Hayes, S. A. H. Guillet, M. Liang, A. L. Aquila, P. R. Willmott, J. S. Robinson, K. L. Gumerlock, S. Botha, K. Nass, I. Schlichting, R. L. Shoeman, H. A. Stone and S. Boutet, *Nat. Phys.*, 2016, **12**, 966–971.

17 G. Nelson, R. A. Kirian, U. Weierstall, N. A. Zatsepin, T. Faragó, T. Baumbach, F. Wilde, F. B. Niesler, B. Zimmer, I. Ishigami, M. Hikitia, S. Bajt, S. Yeh, D. Rousseau, H.

Chapman, J. Spence and M. Heymann, *Opt. Express*, 2016, **24**, 11515–11530.

18 R. Nazari, S. Zaare, R. C. Alvarez, K. Karpos, T. Engelman, C. Madsen, G. Nelson, J. C. Spence, U. Weierstall and R. J. Adrian, *et al.*, *Opt. Express*, 2020, **28**, 21749–21765.

19 J. Knoška, L. Adriano, S. Awel, K. R. Beyerlein, O. Yefanov, D. Oberthuer, G. E. P. Murillo, N. Roth, I. Sarrou and P. Villanueva-Perez, *et al.*, *Nat. Commun.*, 2020, **11**, 1–12.

20 D. Wang, U. Weierstall, L. Pollack and J. Spence, *J. Synchrotron Radiat.*, 2014, **21**, 1364–1366.

21 G. D. Calvey, A. M. Katz, C. B. Schaffer and L. Pollack, *Struct. Dyn.*, 2016, **3**, 054301.

22 R. B. Doak, J. C. Spence, U. Weierstall, D. DePonte, D. Starodub and J. S. Warner, Gas Dyqanamic Virtual Nozzle for Generation of Microscopic Droplet Streams, *US Pat.*, 8272576, 2012.

23 R. B. Doak, R. Shoeman, S. Botha and I. Schlichting, Method and Device of Producing an Intermittent Liquid Jet, *US Pat.*, 9839922, 2017.

24 P. Martien, S. Pope, P. Scott and R. Shaw, *Phys. Lett. A*, 1985, **110**, 399–404.

25 B. Ambravaneswaran, S. D. Phillips and O. A. Basaran, *Phys. Rev. Lett.*, 2000, **85**, 5332.

26 C. Clanet and J. C. Lasheras, *J. Fluid Mech.*, 1999, **383**, 307–326.

27 M. A. Herrada, A. M. Ganán-Calvo, A. Ojeda-Monge, B. Bluth and P. Riesco-Chueca, *Phys. Rev. E*, 2008, **78**, 036323.

28 U. Weierstall, J. C. H. Spence and R. B. Doak, *Rev. Sci. Instrum.*, 2012, **83**, 035108.

29 F. H. Harlow and A. A. Amsden, *J. Comput. Phys.*, 1968, **3**, 80–93.

30 R. Adak, *PhD Thesis*, IIT Bombay, 2021.

31 H. Jasak, *47th AIAA Aerospace Sciences Meeting Including the New Horizons Forum and Aerospace Exposition*, 2009, p. 341.

32 J. Roenby, H. Bredmose and H. Jasak, *R. Soc. Open Sci.*, 2016, **3**, 160405.

33 R. Nazari, A. Ansari, M. Herrmann, R. J. Adrian and R. A. Kirian, *Front. Mech. Eng.*, 2023, **8**, 958963.

34 A. Ansari, *MSc Thesis*, Arizona State University, 2019.

35 J. U. Brackbill, D. B. Kothe and C. Zemach, *J. Comput. Phys.*, 1992, **100**, 335–354.

36 K. Karpos, S. Zaare, D. Manatou, R. C. Alvarez, V. Krishnan, C. Ottmar, J. Gilletti, A. Pableo, D. Doppler, A. Ansari, R. Nazari, A. Ros and R. A. Kirian, *Struct. Dyn.*, 2024, **11**, 064302.

37 R. Zahoor, S. Bajt and B. Šarler, *Int. J. Hydromechatronics*, 2018, **1**, 222–237.

38 A. M. Gañán-Calvo, R. González-Prieto, P. Riesco-Chueca, M. A. Herrada and M. Flores-Mosquera, *Nat. Phys.*, 2007, **3**, 737–742.

39 D. Doppler, M. T. Rabbani, R. Letrun, J. Cruz Villarreal, D. H. Kim, S. Gandhi, A. Egatz-Gomez, M. Sonker, J. Chen and F. H. Koua, *et al.*, *J. Appl. Crystallogr.*, 2022, **55**, 1–13.

40 C. A. Stan, D. Milathianaki, H. Laksmono, R. G. Sierra, T. A. McQueen, M. Messerschmidt, G. J. Williams, J. E. Koglin, T. J. Lane, M. J. Hayes, M. J. Hayes, S. A. H. Guillet, M. Liang, A. L. Aquila, P. R. Willmott, J. S. Robinson, K. L. Gumerlock, S. Botha, K. Nass, I. Schlichting, R. L. Shoeman, H. A. Stone and S. Boutet, *Nat. Phys.*, 2016, **12**, 966.

41 A. Kalita, M. Mrozek-McCourt, T. F. Kaldawi, P. R. Willmott, N. D. Loh, S. Marte, R. G. Sierra, H. Laksmono, J. E. Koglin and M. J. Hayes, *et al.*, *Nature*, 2023, **620**, 557–561.

42 M. Faubel, S. Schlemmer and J. Toennies, *Z. Phys. D: At., Mol. Clusters*, 1988, **10**, 269–277.

43 D. M. Jennewein, J. Lee, C. Kurtz, W. Dizon, I. Shaeffer, A. Chapman, A. Chiquete, J. Burks, A. Carlson and N. Mason, *et al.*, *Practice and Experience in Advanced Research Computing*, ACM Digital Library, 2023, pp. 296–301.

44 A. Volk and C. J. Kähler, *Exp. Fluids*, 2018, **59**, 75.